Continuous-Control-Set Model-Free Predictive Fundamental Current Control for PMSM System

Fengxiang Wang, *Senior Member, IEEE*, Yao Wei, *Member, IEEE*, Hector Young, *Senior Member, IEEE*, Dongliang Ke, *Senior Member, IEEE*, Haotian Xie, *Member, IEEE*, and José Rodríguez, *Life Fellow, IEEE*

***Abstract*—Although the robustness is enhanced essentially by the model-free predictive control, the accuracy of its data-driven model is directly affected by the unnecessary current harmonics, such as the harmonics caused by the control strategy itself. To reduce the influences of these harmonics, a continuous-control-set model-free predictive fundamental current control (MF-PFCC) strategy is proposed in this article for the permanent magnet synchronous motor driving system. Harmonics due to the controller including side frequency effect and frequency coupling effect are analyzed in principle, and a frequency-converting double second-order generalized integrator structure is designed to exclude the fundamental terms from the sampled current to cut the coupling path of the effects and to improve the accuracy of the data-driven model in the MF-PFCC without any time-variable physical parameters. The analyses of the effects and the effectiveness of the proposed method are verified by experimental and supplementary simulation results, as well as advantages including the reduced influence of effects and enhanced robustness with improved stator current quality.**

***Index Terms*—Current harmonics, frequency-converting double second-order generalized integrator (DSOGI), fundamental terms, model-free predictive control.**

I. Introduction

THE permanent magnet synchronous motor (PMSM) has advantages including less volume, higher power density, and larger torque, and is often considered for industry applications in harsh environments. With the development of the applications, the requirement for the control strategy becomes more strict in the electrical driving realm. Model predictive control (MPC) strategy is widely focused due to its excellent dynamics, good compatibility of the multiple objectives, easy understanding, and operation [1], [2]. According to the implementation modes of the MPC, it is divided into the following: 1) continuous-control-set (CCS) MPC; 2) finite-control-set MPC. The former requires a modulator to generate pulses with fixed switching frequency and the latter is realized based on the candidate vector table with variable switching frequency [3]. MPC can also be divided into predictive current control (PCC), predictive speed control, and predictive torque control (PTC) mainly according to the primary objective of the motor control system [4].

Since some physical parameters of the motor are nonlinear time-varying, the system is always operating under the condition of parameter mismatches and the weak robustness is a serious problem for the MPC strategy [5]. Research efforts have addressed different aspects, including elimination of weighting factors [6], prolonged prediction horizon [7], and the design of observers, trying to solve this problem. Since the accurate variables and online adjust the model of the MPC are obtained by the observer, it is an effective method to enhance the robustness. Based on the typical structures such as disturbance observer, linear extended state observer (ESO), and Luenberger observer [8], [9], some advanced observers are designed to estimate the variables. An integral sliding mode observer (SMO) is presented respectively to improve estimating accuracy [10], and an extended high-gain state observer is used to suit a variety of loads without integral term [11]. A parallel ESO structure is designed to consider both the system behavior prediction and disturbance estimation simultaneously [12].

Building a data-driven model is an effective consideration to solve the problem of weak robustness essentially because this model is directly built by the sampled data and the dependence on the physical parameters is fully eliminated [13]. There are three typical structures including full-form dynamic linearization, ultralocal and auto-regressive with exogenous input (ARX) that are selected to design a data-driven model. The first one is a composite of the compact-form and partial-form dynamic linearizations used to estimate the plant, and the model adaptive predictive control is presented to build a data-driven model [14]. The known and unknown parts of the plant are summarized and replaced by a variable for the one-order ultralocal structure and approximated by the mathematical optimization or observer [15]. An ESO is used to estimate the above-mentioned variable to resist parameter mismatches and converted as the voltage objectives to realize the CCS type [16], and the required number of parameters is further reduced in [17]. The full-order

Manuscript received 30 June 2022; revised 21 October 2022 and 6 December 2022; accepted 21 January 2023. Date of publication 27 January 2023; date of current version 10 March 2023. The work of José Rodríguez was supported by ANID through Projects FB0008, 1210208, and 1221293. This work was supported in part by the National Natural Science Funds of China under Grant 52277070, in part by Project FRO19101 MINEDUC. Recommended for publication by Associate Editor H. Hofmann. *(Corresponding author: Yao Wei.)*

Fengxiang Wang, Yao Wei, and Dongliang Ke are with the Quanzhou Institute of Equipment Manufacturing, Haixi Institutes, Chinese Academy of Sciences, Jinjiang 362200, China (e-mail: fengxiang.wang@fjirsm.ac.cn; wei@fjirsm.ac.cn; dongliang.ke@fjirsm.ac.cn).

Hector Young is with the Department of Electrical Engineering, Universidad de La Frontera, Temuco 4811230, Chile (e-mail: hector.young@ufrontera.cl).

Haotian Xie is with the Chair of High-Power Converter Systems, Technical Unversity of Munich, 80333 Munich, Germany (e-mail: haotian.xie@tum.de).

José Rodríguez is with the Faculty of Engineering, Universidad San Sebastian, Santiago 8370146, Chile (e-mail: jose.rodriguezp@uss.cl).

Color versions of one or more figures in this article are available at https://doi.org/10.1109/TPEL.2023.3240282.

Digital Object Identifier 10.1109/TPEL.2023.3240282

SMO also can be applied to estimate the total disturbance of the ultralocal structure to further enhance the robustness, and two vectors are applied in each sampling period to reduce the current ripple [18]. The ARX structure makes the plant approximate as a group of transfer functions, and their coefficients are online calculated by the recursive least square algorithm [19]. The input and output variables for the multiple-input multiple-output system are decoupled and an accurate model of the plant is achieved by this structure [20]. But this structure is not widely applied in the industry for now due to its heavy requirement for processor resources.

Since some plants have no information about the sampled data and hard to determine a suitable typical structure, some artificial intelligence algorithms, such as artificial neural network [21] and recurrent neural network [22], are adapted to generate a data-driven model of the black box plant.

To solve the harmonic control issue, an improved switching table is designed to preselect the vectors with reduced stator flux in the *x*–*y* subspace to suppress the stator harmonic current in the predictive control [23]. A deadbeat PCC based on adaptive harmonic reference correcting current injection method is presented in [24] to compensate for the harmonics caused by the inverter nonlinearity and back electromotive force (EMF). A virtual-vector-based model predictive current control (MPCC) is proposed in [25], and the 3rd harmonic is reduced by controlling the proportion of medium vector and large vector reasonably. A similarly improved modulation is also proposed in [26] to reduce low-order harmonics.

Since some harmonics are generated by the control strategy itself, such as the harmonic coupling effect and side frequency effect [27], [28], the quality of the data-driven model is directly influenced by these harmonics, and the sampled data should be cleaned to reduce their influences. The typical second-order generalized integrator (SOGI) in [29] and [30] is used to lock the phase or frequency and to estimate speed or position in the sensorless system, as well as the flux linkage [31], and this structure has enough potential to clean the sampled data and achieve an accurate data-driven model in the model-free predictive control. A model-free predictive fundamental current control (MF-PFCC) strategy is proposed in this article and applied to a PMSM speed control system. The harmonics caused by the control strategy are analyzed, including the frequency coupling effect and side frequency effect, and a frequency-converting double SOGI (DSOGI) structure without any time-variable physical parameters is designed to reduce the influences of these effects and to improve the data-driven model accuracy. The effectiveness of the proposed method and the advantages of the reduced influences of the effects and enhanced robustness with better stator current quality are demonstrated by the experimental and supplementary simulation results compared to the MF-PCC strategy in [17].

The rest of this article is organized as follows. The PMSM model and its basic PCC strategy are briefly introduced in Section II. The harmonics caused by the control strategy are analyzed in Section III, and the MF-PFCC strategy is presented based on the frequency-converting DSOGI structure in Section IV and applied to the PMSM speed control system. Compared with the MF-PCC, the experimental validations are expressed to demonstrate the obtained performances and current quality in Section V. Finally, Section VI concludes this article.

II. PMSM Model and PCC

A. PMSM Model

The model of PMSM is expressed as the following expressions including stator voltage v_s, electrical torque T_e, and stator flux linkage ψ_s

$$\begin{cases} v_{sd} = R_s i_{sd} + L_{sd}\frac{di_{sd}}{dt} - L_{sq}\omega_r i_{sq} \\ v_{sq} = R_s i_{sq} + L_{sq}\frac{di_{sq}}{dt} + L_{sd}\omega_r i_{sd} + \omega_r \psi_m \end{cases} \tag{1}$$

$$\begin{cases} \psi_{sd} = L_{sd} i_{sd} + \psi_m \\ \psi_{sq} = L_{sq} i_{sq} \end{cases} \tag{2}$$

$$T_e = p[\psi_m i_{sq} + (L_{sd} - L_{sq}) i_{sd} i_{sq}] \tag{3}$$

where the subscript d and q are the components on d-axis and q-axis of a synchronous reference frame, respectively; R_s is the stator resistance, L_s is the stator inductance, ψ_m is the magnet flux linkage, p is the number of pole pairs, and ω_r is the electrical angular velocity.

An equation of motion for PMSM is

$$\frac{d\omega_r}{dt} = \frac{p}{J}(T_e - T_L) - \frac{B}{J}\omega_r \tag{4}$$

where T_L is the load torque, J is the inertia coefficient, and B is the viscosity coefficient of PMSM.

The discrete-time model of the PMSM is obtained based on the Euler algorithm and sampling period T_s, and the stator current components are predicted for the $(k+1)$th sampling period.

B. CCS-PCC Strategy

According to the objectives for the PCC strategy, the cost function is designed as

$$J = (i_{sd}(k+1))^2 + \lambda(i_{sq}(k+1) - i_{sq}^*)^2 \tag{5}$$

where i_{sq}^* is the reference of i_{sq} and λ is the weighting factor which is tuned by the branch and bound algorithm in [32]. The two terms in the cost function make the components of the current follow their references.

To find the optimal control action, substitute the model into the cost function and solve the derivative with respect to the stator voltage u_s as zero, i.e.,

$$\frac{dJ}{du_{sd}} = 0, \frac{dJ}{du_{sq}} = 0 \tag{6}$$

and the stator voltage is expressed as follows to generate pulses to control the motor driver:

$$\begin{cases} u_{sd} = \left(R_s - \frac{L_{sd}}{T_s}\right) i_{sd} - L_{sd} i_{sq} \omega_r \\ u_{sq} = \left(R_s - \frac{L_{sq}}{T_s}\right) i_{sq} + L_{sq} i_{sd} \omega_r + L_{sq}\psi_m \omega_r + \frac{L_{sq}}{T_s} i_{sq}^*. \end{cases} \tag{7}$$

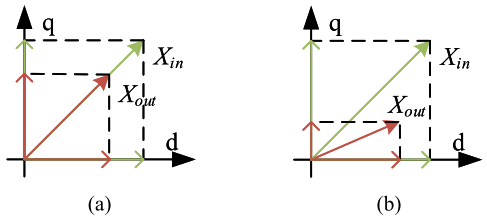

Fig. 1. Space vectors of the input and output signals. (a) Symmetric strategy. (b) Asymmetric strategy.

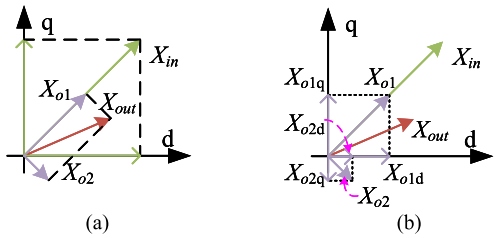

Fig. 2. Divided processes of the lagging output vector. (a) Input vector and its orthometric directions. (b) dq-axis.

Based on the cost function in (5), the required stator voltages have the minimum gradient and it can be seen as an equality-constrained optimization process

$$\min f = ||\boldsymbol{x}^* - \boldsymbol{x}(k+1)||_2^2 + ||\boldsymbol{S}(k+1) - \boldsymbol{S}(k)||_2^2$$
$$\begin{cases} \text{s.t. } \boldsymbol{x}(k+1) = \boldsymbol{A}(k)\boldsymbol{x}(k) + \boldsymbol{B}(k)\boldsymbol{u}(k) \\ \quad ||\boldsymbol{U}(k)||_2 \le U_L, ||\boldsymbol{x}(k)||_2 \le C_L \end{cases} \tag{8}$$

where $\boldsymbol{U}$ is a set of candidate voltages, U_L is the limitation for the voltage, and C_L is the limitation for the current. The second term about $\boldsymbol{S}$ in the first formula is a penalty.

The Lagrangian function is defined as

$$L(\boldsymbol{x}, \lambda,' \mu_1, \mu_2) = f + \lambda'[(\boldsymbol{A} - \boldsymbol{I})\boldsymbol{x} + \boldsymbol{B}\boldsymbol{u}] + \mu_1(||\boldsymbol{U}||_2 - U_L) + \mu_2(||\boldsymbol{x}||_2 - C_L) \tag{9}$$

and its Karush–Kuhn-Tucker (KKT) conditions are

$$\begin{cases} \frac{\partial L}{\partial x_i} = 0, x = 1, 2 \\ (\boldsymbol{A} - \boldsymbol{I})\boldsymbol{x} + \boldsymbol{B}\boldsymbol{u} = 0 \\ ||\boldsymbol{U}||_2 - U_L \le 0, ||\boldsymbol{x}||_2 - C_L \le 0 \\ \mu_1 \ge 0, \mu_2 \ge 0 \\ \mu_1(||\boldsymbol{U}||_2 - U_L) = 0, \mu_2(||\boldsymbol{x}||_2 - C_L) = 0 \end{cases} \tag{10}$$

where $\boldsymbol{A}$ and $\boldsymbol{B}$ are the state matrices, $\boldsymbol{x} = [x_1, x_2]^T$ means the current components, and λ', μ_1, and μ_2 are the KKT multipliers.

Since the matrix $\boldsymbol{A}$ is full rank, all KKT conditions are satisfied through the matrix calculations, and the cost function has a solution. A maximum modulation ratio and a limitation of current reference are preset to implement voltage and current constraints, respectively. These constraints allow to achieve a good control performance and their inclusion in the control algorithm is possible with a suitable calculation burden for online implementation.

III. Harmonic Effects in PCC

Besides the harmonics caused by the motor such as the distorted magnetic field and cogging torque, some harmonics are also generated and affected by the control strategy because of its specific property, as discussed later in this section.

A. Asymmertric Property and Frequency Coupling Effect

As shown in Fig. 1, the d- and q-components of the stator current are the same if their controllers are symmetric, and a difference appears between the phases of the input and output signals if these controllers are asymmetric. The MF-PCC strategy belongs to the latter according to its model and cost function. Due to the asymmetric property, the output signal can be divided based on the same direction and the orthorhombic direction of the input signal, as shown in Fig. 2. Defining the components in the two directions as X_{o1} and X_{o2}, they are expressed as follows

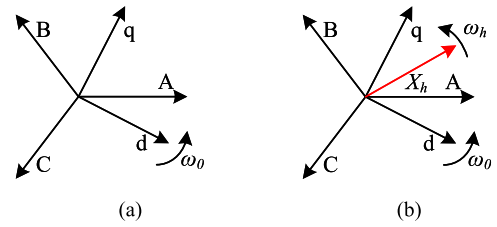

Fig. 3. Vector table of PMSM. (a) Normal operation. (b) Operation with harmonic.

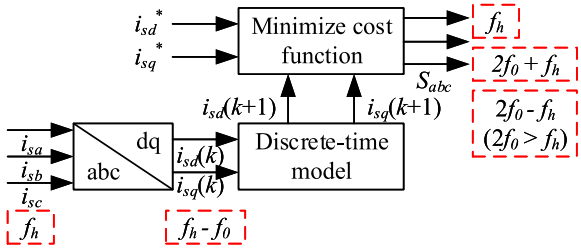

Fig. 4. Sketch of the frequency coupling effect.

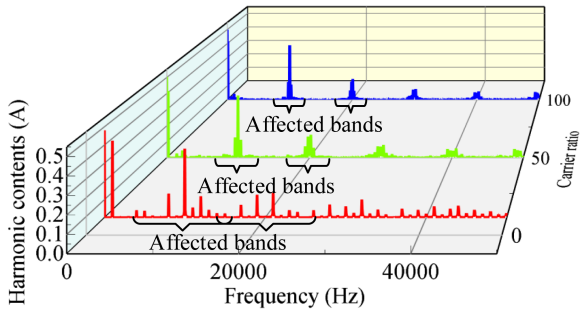

Fig. 5. Sketch of the side frequency effect.

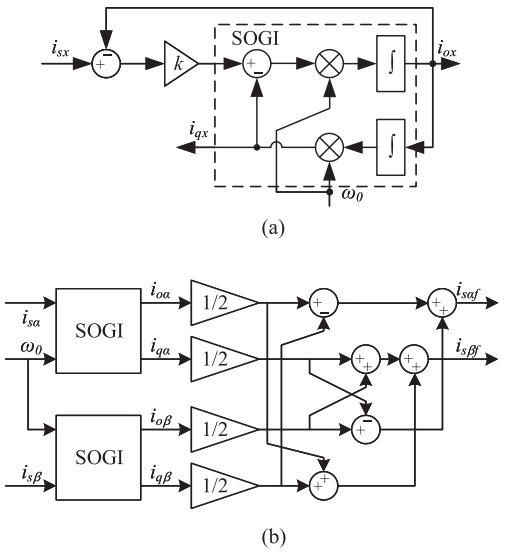

Fig. 6. Structure of frequency-converting DSOGI. (a) SOGI. (b) DSOGI.

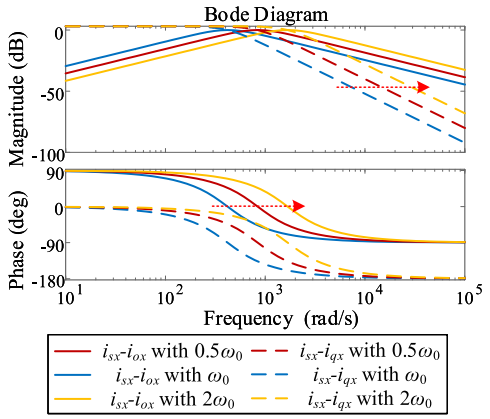

Fig. 7. Bode diagram of the frequency-converting DSOGI.

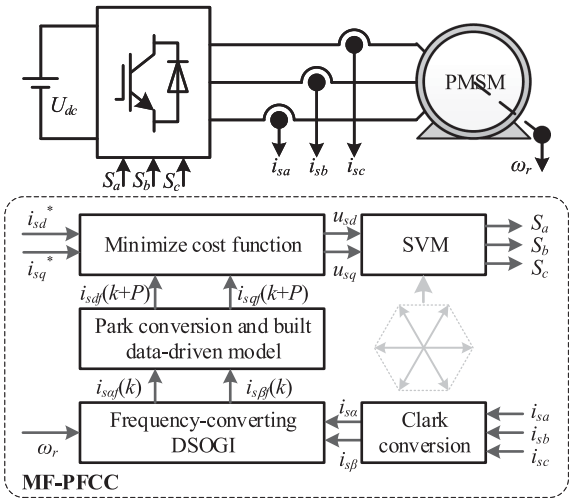

Fig. 8. System structure of the proposed method.

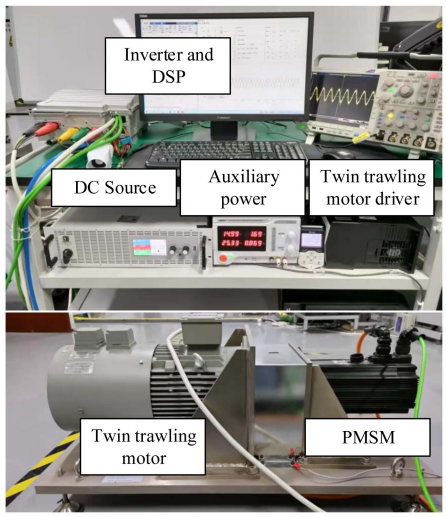

Fig. 9. Experimental platform.

on the dq-frame:

$$\begin{cases} X_{o1} = X_{o1d} + jX_{o1q} \\ X_{o2} = X_{o2d} \pm jX_{o2q} \end{cases} \tag{11}$$

and

$$X_{\text{out}} = X_{o1} + X_{o2} = X_{o1d} + X_{o2d} + j(X_{o1q} \pm X_{o2q}) \tag{12}$$

where the output vector might be leading or lagging compared with the input vector since the minimum gradient of the error between the vectors is required for the PCC strategy. The positive signs in the equations are satisfied if the output vector is leading, and the negative signs are satisfied on the contrary. It can be seen that a harmonic is generated by the asymmetric property, and this phenomenon is called frequency coupling effect. The content and rotating direction of the generated harmonic are directly affected by the relative angle between the input and output vectors.

According to the model of PMSM, its space vectors are shown in Fig. 3(a) when the motor is operating normally, and the vectors are changed as Fig. 3(b) if a harmonic with frequency f_h is inserted in the system. The harmonic frequencies for each term of the PCC strategy are shown in Fig. 4. The frequency of inserted harmonic is changed as $f_h - f_0$ after the Clark and Park transformations. Since the output vector is operated on the abc coordinate, the harmonic frequencies reflected on this coordinate are f_h, $2f_0 + f_h$, and $2f_0 - f_h$ after the controller, where the last harmonic appears if $2f_0 > f_h$ is satisfied in principle.

B. Side Frequency Effect

The harmonics whose frequencies are equal to the carrier frequency and its integral multiple are generated in the modulator due to the side frequency effect. A Fourier analysis result of the pulse width modulation is shown in Fig. 5 as an example. The affected bands of the carrier frequency and its integer multiple frequencies are growing wider with the decrement of the carrier ratio, i.e., operating within the high-speed range for the motor

TABLE I
MAIN PARAMETERS OF THE PLATFORM

Symbols	Quantity	Values
R_s	Stator resistance	0.637 Ω
L_{sd}	Stator inductance on d-axis	10 mH
L_{sq}	Stator inductance on q-axis	14.5 mH
p	The number of pole pair	4
ψ_m	Magnet flux linkage	0.31 Wb
J	Rotor inertia	0.005 kg.m^2
$U_{\rm dc}$	DC voltage	540 V
T_s	Sampling period	62.5 μs
ω	Required bandwidth	8500 rd/s
k	Resonance coefficient	2.5
K_p	Proportional coefficient	750
λ	Weighting factor	2

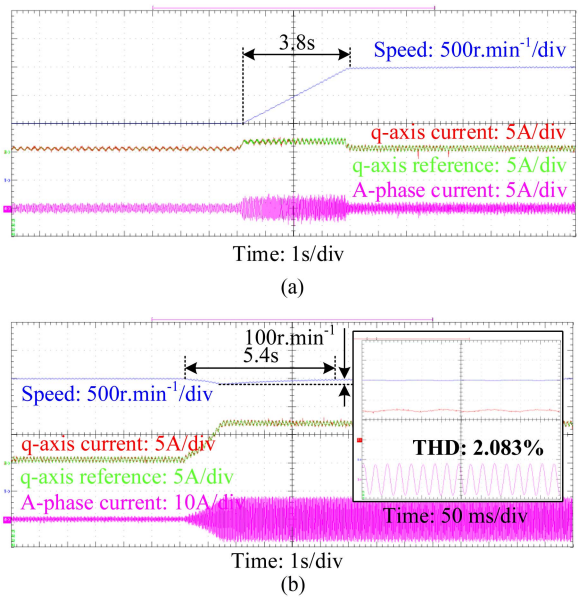

Fig. 10. Experimental waveforms of the proposed method. (a) Reference changing process. (b) Disturbance resisting process.

driving system with a fixed switching frequency. These bands intrude into their neighbors and the left side of the carrier band enters into the required signal band when the carrier ratio is small enough, and these harmonics influence the quality of the data-driven model.

Considering the inherent harmonics caused by the motor, the A-phase stator current of PMSM with the harmonics is

$$i_{sa} = i_f \sin(\omega_0 t + \theta_0) + i_5 \sin(-5\omega_0 t + \theta_1) + i_7 \sin(7\omega_0 t + \theta_2) + \cdots \tag{13}$$

and the B and C phases of the stator current have similar expressions with different phases, where θ_0, θ_1, and θ_2 are the initial phases of the fundamental and harmonics; i_5 and i_7 in the last two terms are the magnitudes for the 5th and 7th harmonics, respectively. Due to the asymmetric property and repetitive frequency coupling effects, more harmonics are generated and brought into the current by the existing harmonics including the inherent harmonics and harmonics of the side frequency effect mainly.

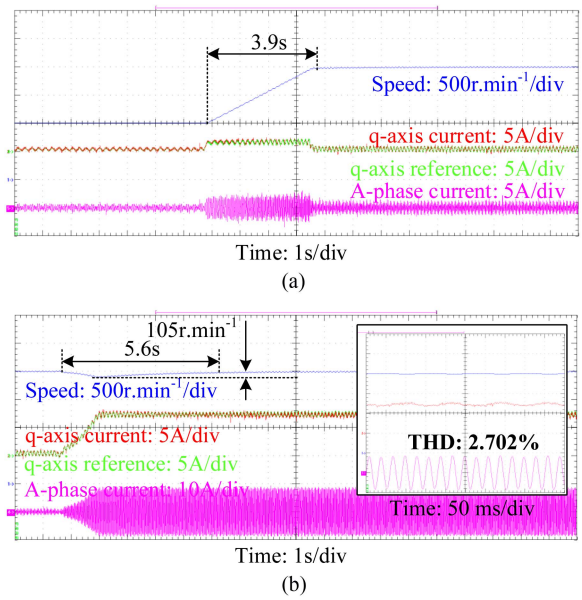

Fig. 11. Experimental waveforms of the MF-PCC strategy. (a) Reference changing process. (b) Disturbance resisting process.

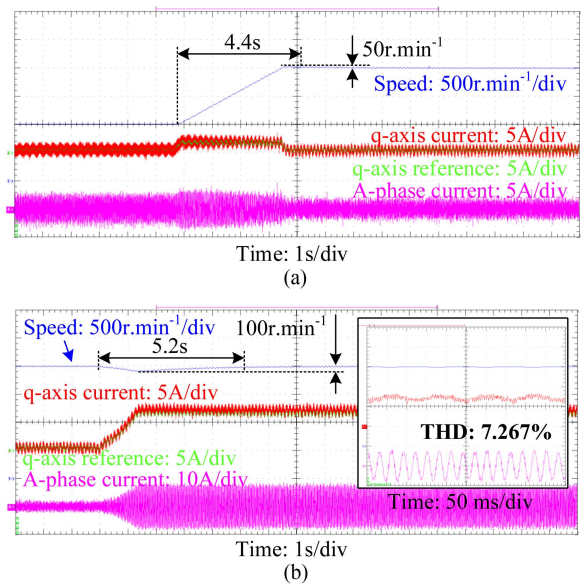

Fig. 12. Experimental waveforms of the CCS-PCC strategy. (a) Reference changing process. (b) Disturbance resisting process.

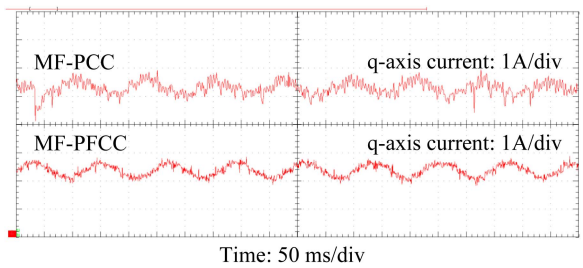

Fig. 13. Enlarged q-axis currents of MF-PFCC and MF-PCC strategies.

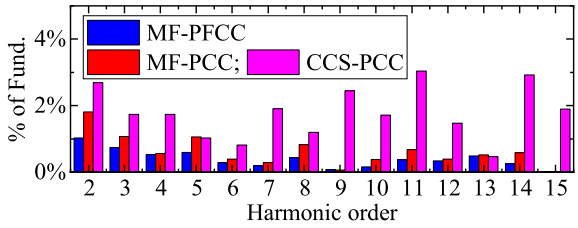

Fig. 14. Fourier analysis results of the sampled phase currents for different control strategies.

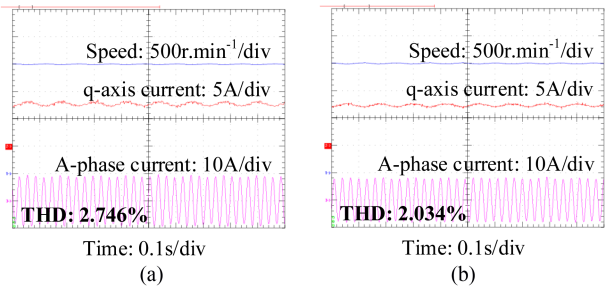

Fig. 15. Experimental waveforms with parameter mismatches of $R_{se}/R_s = 0.1$, $L_{se}/L_s = 0.5$, and $\psi_{me}/\psi_m = 2$. (a) MF-PCC. (b) MF-PFCC.

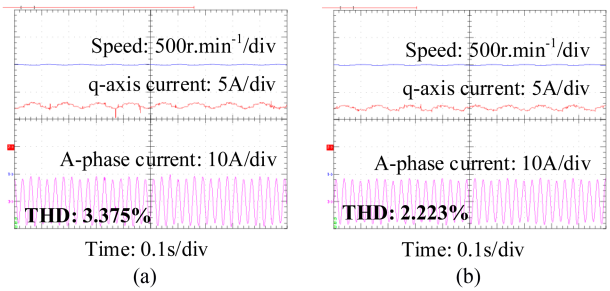

Fig. 16. Experimental waveforms with parameter mismatches of $L_{se}/L_s = 2$ and $\psi_{me}/\psi_m = 2$. (a) MF-PCC. (b) MF-PFCC.

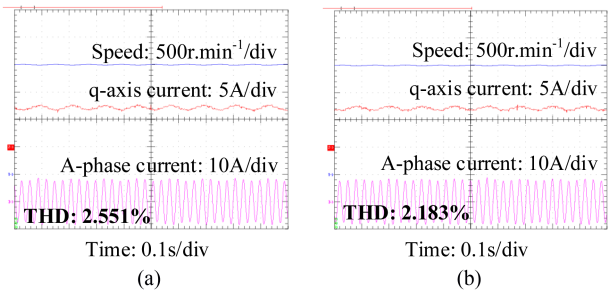

Fig. 17. Experimental waveforms with parameter mismatches of $R_{se}/R_s = 10$, $L_{se}/L_s = 2$, and $\psi_{me}/\psi_m = 0.7$. (a) MF-PCC. (b) MF-PFCC.

IV. MF-PFCC With Cleaned Sampled Data

A. Cleaned Sampled Data by Frequency-Converting DSOGI

The structure of the frequency-converting DSOGI is shown in Fig. 6, and it can be expressed as

$$\begin{cases} i_{ox} = \frac{k\omega_0 s}{s^2+k\omega_0 s+\omega_0^2} i_{sx} \\ i_{qx} = \frac{k\omega_0^2}{s^2+k\omega_0 s+\omega_0^2} i_{sx} \end{cases} \tag{14}$$

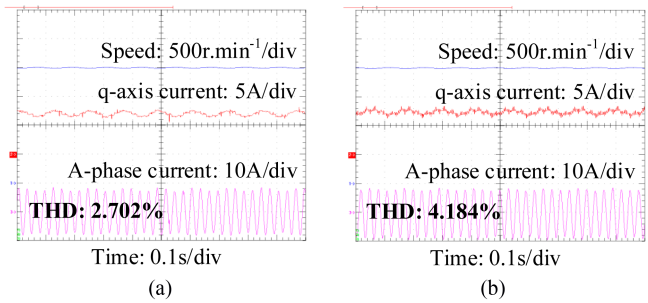

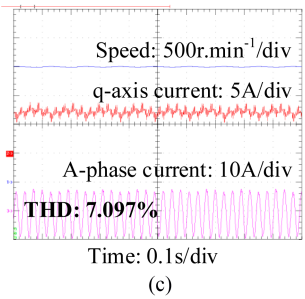

Fig. 18. Experimental waveforms with different amplitudes of the inserted harmonics. (a) MF-PCC with 0.5 A amplitude. (b) MF-PCC with 1 A amplitude. (c) MF-PCC with 2 A amplitude.

where the subscript x means the component is on the α or β axis, i_{ox} and i_{qx} are the output and its quadrature signal of the SOGI, respectively, k is the resonance coefficient, and ω_0 is the angular frequency of fundamental, which is satisfied as

$$\omega_0 = 2\pi f_0 = \frac{p\pi}{30} n \tag{15}$$

where n is the rotor speed in r/min.

The bode diagram of the frequency-converting DSOGI in (14) is shown in Fig. 7 when ω_0 is fixed. It shows that the break frequency is moving right with the increment of the angular frequency of the fundamental, and the passed band is tracking the fundamental continuously to extract the harmonics.

B. Proposed Control Strategy

Since a large number of calculation processes are required in the actuation, the prediction horizon P is prolonged to compensate these delays. The following one-order ultralocal structure is selected to estimate the harmonic influence:

$$\frac{d\boldsymbol{i}_{sf}}{dt} = \boldsymbol{F} + \alpha \boldsymbol{u}_s \tag{16}$$

where $\boldsymbol{i}_{sf} = [i_{sdf}, i_{sqf}]^T$, $\boldsymbol{u}_s = [u_{sd}, u_{sq}]^T$, α is the proportional coefficient, and F is the estimated part including all of the known and unknown terms of the plant.

The following linear ESO is designed to estimate $\boldsymbol{i}_{sf}$ and $\boldsymbol{F}$, i.e., defined $z_1 = \widehat{\boldsymbol{i}}_{sf}$, $z_2 = \widehat{\boldsymbol{F}}$:

$$\begin{cases} \boldsymbol{e} = \boldsymbol{z}_1(k) - \boldsymbol{i}_{sf} \\ \boldsymbol{z}_1(k+1) = \boldsymbol{z}_1(k) + T_s(\boldsymbol{z}_2(k) + \alpha \boldsymbol{u}_s - \beta_1 \boldsymbol{e}) \\ \boldsymbol{z}_2(k+1) = \boldsymbol{z}_2(k) - T_s \beta_2 \boldsymbol{e} \end{cases} \tag{17}$$

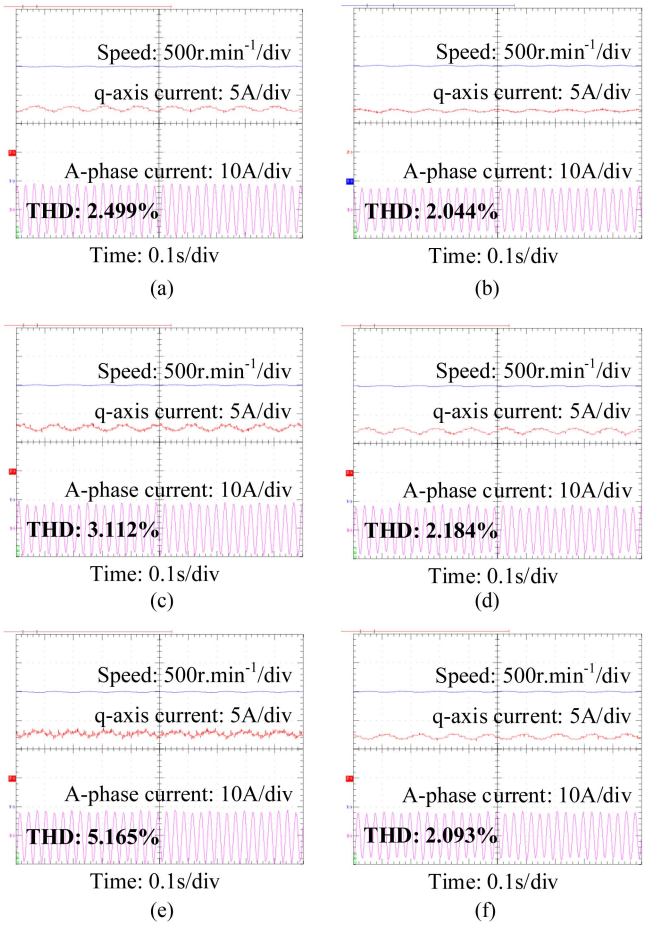

Fig. 19. Experimental waveforms of MF-PFCC strategy with different amplitudes of the inserted harmonics. (a) Sampled currents with inserted harmonic of 0.5 A amplitude. (b) Cleaned currents with inserted harmonic of 0.5 A amplitude. (c) Sampled currents with inserted harmonic of 1 A amplitude. (d) Cleaned currents with inserted harmonic of 1 A amplitude. (e) Sampled currents with inserted harmonic of 2 A amplitude. (f) Cleaned currents with inserted harmonic of 2 A amplitude.

where β_1 and β_2 are the feedback gains which can be calculated by the required bandwidth ω

$$\begin{cases} \beta_1 = 2\omega \\ \beta_2 = \omega^2. \end{cases} \tag{18}$$

Based on the Lagrange interpolation algorithm, the reference $\boldsymbol{i}_s^*$ is predicted to the Pth sampling period. Considering calculation delay in the digital implementation, assuming the fundamental reaches its reference at the next sampling period, the output voltage $\boldsymbol{u}_s$ is

$$\boldsymbol{u}_s = \frac{1}{\alpha}\left(-\widehat{\boldsymbol{F}}(k+P) + \frac{d\boldsymbol{i}_s^*(k+P+1)}{dt}\right) + \frac{K_p}{\alpha}(\boldsymbol{i}_s^*(k+P+1) - \widehat{\boldsymbol{i}}_{sf}(k+P)) \tag{19}$$

where $\boldsymbol{i}_s^* = [i_{sd}^*, i_{sq}^*]^T$, and K_p is the proportional coefficient. The derivative in the equation is computed by the Euler approximation. The prediction horizon P is selected as 2 based on the computation delays. A space vector modulation is used to generate the pulses.

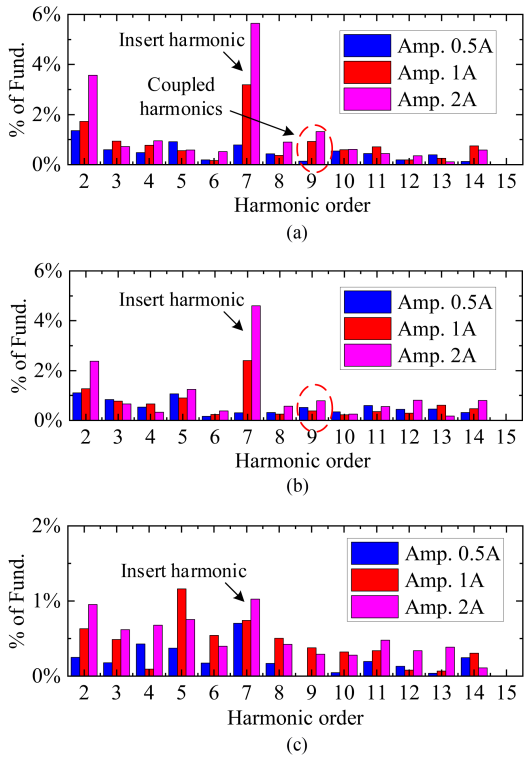

Fig. 20. Fourier analysis results of the phase currents with different amplitudes of the inserted 7th harmonics. (a) Sampled currents of MF-PCC. (b) Sampled currents of MF-PFCC. (c) Cleaned currents of MF-PFCC.

The structure of the proposed method is shown in Fig. 8, and it is located between the sampling process and predictive controller to clean the sampled data. Based on the frequency-converting DSOGI structure, all of the fundamental within the sampled current is extracted to online build the data-driven model, and the achieved model is not affected by the harmonics and their frequency coupling effect. Moreover, the calculation process of the proposed method does not need any time-variable physical parameters of the plant to ensure robustness, where p is a constant value in (15).

V. Experimental Validations

According to the structure in Fig. 8, a platform is built based on a 4.8-kW PMSM and a DSP F28379D as shown in Fig. 9. The parameters of the platform are listed in Table I, where k and K_p are determined by the branch and bound algorithm.

A. Tracking Performance

The initial speed reference is set 1000 r/min. The speed reference is step changed to 2000 r/min, and the load torque is changed from 0 to 11.5 N.m. Experimental waveforms including speed, sampled A-phase current, q-axis current, and its reference are shown in Fig. 10 for the MF-PFCC strategy. It shows that the speed tracks the reference within 3.8 s during the tracking reference process without overshoot and enters into the

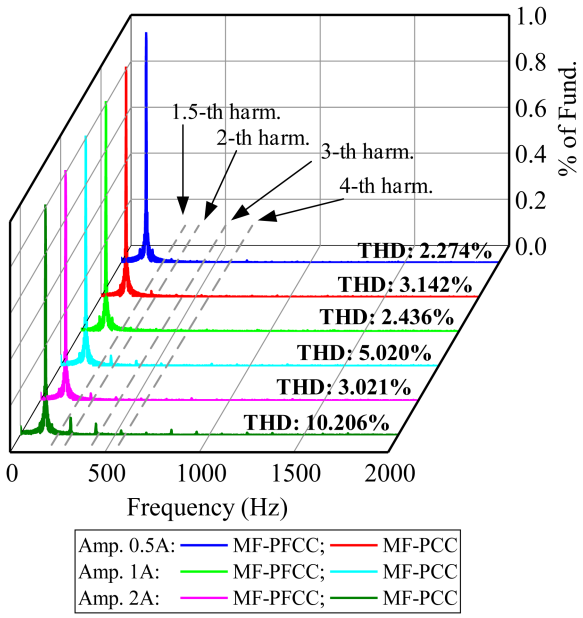

Fig. 21. Continuous Fourier analysis results of the cleaned currents with different amplitudes of the inserted 1.5th harmonics.

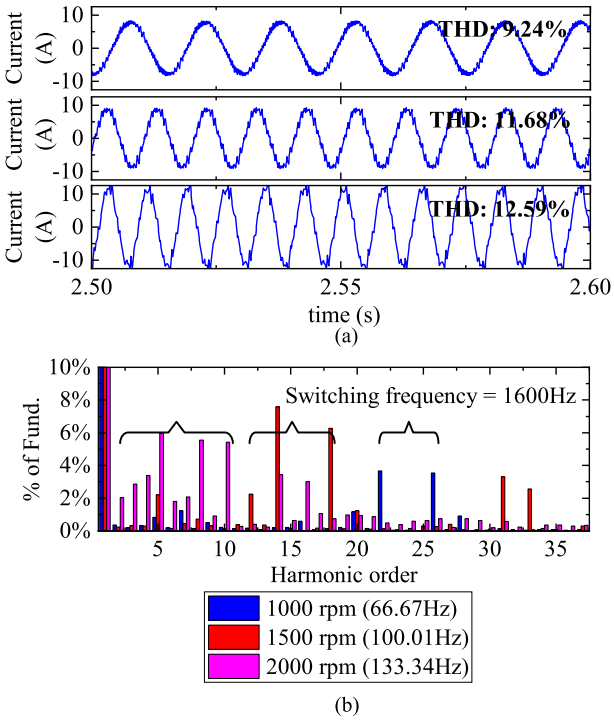

Fig. 22. Simulation waveforms of phase current with different speed references and their fast Fourier transform (FFT) results. (a) Simulation waveforms. (b) FFT results.

steady-state. During the disturbance resisting process, the speed has an overshoot of about 10% and returns to the steady-state within about 5.5 s. The system can track the reference and resist the disturbance successfully and the total harmonic distortion (THD) of the sampled phase current is 2.702%.

TABLE II
TYPICAL INDEXES OF CONTROL PERFORMANCE

Index	MF-PFCC	MF-PCC	CCS-PCC
Settling time within reference changing process	3.8s	3.9s	4.4s
Overshoot of reference changing process	-	-	2.5%
Settling time within disturbance resisting process	5.4s	5.6s	5.2s
Overshoot of reference changing process	5.0%	5.25%	5.0%
Sampled phase current THD	2.083%	2.702%	7.267%
Speed ITAE	10.861	11.653	12.116

Under the same conditions, the experimental waveforms of the MF-PCC with ESO in [17] and CCS-PCC strategies are shown in Figs. 11 and 12, respectively. The settling times are 3.9 and 5.6 s for the MF-PCC strategy during these two transient-states, and the overshoot is about 105 r/min during the disturbance resisting process. The settling times during these two transient-states are 4.4 and 5.2 s for the CCS-PCC strategy, and the overshoots both appear during the two states, which are about 50 and 100 r/min. THDs of the sampled phase currents are 2.702% and 7.267% for these two strategies.

During the steady-state, the q-axis currents of the proposed method and MF-PCC strategy in Figs. 10 and 11 are enlarged and shown in Fig. 13 to provide more detail. It shows that some high-frequency ripples are obviously decreased by the proposed method due to the decreased harmonic contents by the improved model accuracy and reduced harmonic coupling effect.

The Fourier analysis results of the A-phase currents for these three strategies are shown in Fig. 14, where the 3rd and its integral-times order harmonics are not fully eliminated as the platform is not exactly symmetric. The main low-order harmonics, such as 5th and 7th harmonics, are reduced due to the accurate model. The even-order harmonics, such as 2nd, 4th, and 6th harmonics, are also reduced since these harmonics are always aggravated by the mechanical vibration which is caused by the harmonics with all kinds of parameters.

Some typical indexes of control performance are summarized in Table II, where the speed integrated time and absolute errors (ITAEs) are obtained by the continuous 2000 sampled points. It shows that the dynamics and overshoots of the proposed method are similar to the MF-PCC and better than the CCS-PCC strategy. The sampled phase current THD and the speed ITAE for the proposed method are improved by 29.717% and 6.797%, respectively compared with the MF-PCC strategy.

B. Tolerance of Parameter Mismatches

Define the used physical parameter values including R_s, L_s, and ψ_m in the control strategy as R_{se}, L_{se}, and ψ_{me}, respectively. The experimental waveforms and the sampled phase current THDs under the conditions of $R_{se}/R_s = 0.1$, $L_{se}/L_s = 0.5$, and $\psi_{me}/\psi_m = 2$ with 11.5 N.m load torque are shown in Fig. 15 for the MF-PFCC and MF-PCC strategies, where the second ratio of the stator inductance are applied to the d- and q-axis components at the same time. It shows that the

stator currents for the proposed method have lower THD values and ripples.

Similarly, the experimental waveforms and sampled phase current THDs under the conditions of $L_{se}/L_s = 2$ and $\psi_{me}/\psi_m = 2$ and the conditions of $R_{se}/R_s = 10$, $L_{se}/L_s = 2$ and $\psi_{me}/\psi_m = 0.7$ are shown in Figs. 16 and 17, respectively. These two strategies both have good control performance which is insensitive to parameter mismatches. Due to the accurate data-driven model, the quality of the current is improved compared with the MF-PCC strategy.

C. Performance of Cleaned Currents

Since the generated harmonics by the control strategy cannot be extracted clearly from the sampled stator current, a 7th harmonic is used to simulate the enlarged harmonic caused by the control strategy and inserted into the sampled current. The experimental waveforms with amplitudes of 0.5 A, 1 A, and 2 A are shown in Figs. 18 and 19 for the MF-PCC and proposed strategies respectively, in which the figures on the left side are the sampled currents and the figures on the right side are the cleaned currents of the proposed method. For the previous control strategy, it shows that the current quality is decreased obviously with the increment of the harmonic amplitude according to the increasing ripple of the q-axis current and THD of the A-phase current. For the proposed method, some high-frequency harmonics are reduced obviously in the sampled currents and the current quality of the cleaned currents is not obviously affected by the inserted harmonic because of the frequency-converting DSOGI structure to achieve an accurate data-driven model.

The Fourier analyses of the phase currents are shown in Fig. 20. Compared with the content of the 9th harmonic in Fig. 14, the content has an obvious increment by the increasing amplitude of the inserted harmonic for the MF-PCC because of the frequency coupling effect. For the proposed method, the 9th harmonic contents have no obvious trend with the inserted harmonic in the sampled currents and cleaned currents, and the inserted harmonics are almost completely deleted.

Under the same conditions, the continuous Fourier analysis results of the cleaned currents with 1.5-order inserted harmonic are shown in Fig. 21 where the harmonic contents are analyzed within [0, 2000 Hz]. It shows that all of the integral-order harmonics are affected by the inserted harmonic, but the 1.5th harmonic has no obvious changes for these two strategies, and the $(2f_0 - f_h)$th harmonic is not generated. Moreover, although the 1.5th harmonic cannot be fully filtered due to its location close to fundamental, according to the THDs of the phase currents, influences of the fractional-order harmonics are also reduced because the frequency-converting DSOGI structure is a band-pass filter.

VI. Supplementary Simulation Validations

Because the harmonics caused by the side frequency effect are located in the high-frequency range, they are always flooded by the other harmonics, such as the noises and harmonics due to the motor in the high-speed range, and this effect could be verified by the simulation. A simulation environment is built on MATLAB software based on the parameters in Table I.

The phase-current waveforms and FFT results under the conditions of different speed references are shown in Fig. 22, in which the switching frequency is set to 1600 Hz and the load torque is set to 11.5 N.m to observe easily. Although the FFT results have randomness and are affected by the harmonic coupling effect repeatedly, the tendency of the side frequency effect is that with the increasing speed reference, the current quality is reduced and the affected band is moved left and becomes wider, which satisfies the analysis in Fig. 5.

VII. Conclusion

To improve the data-driven model accuracy of the model-free predictive control in the motor driving system, the MF-PFCC strategy is presented in this article based on the analyses of the harmonic coupling effect and side frequency effect. The fundamental terms are extracted from the sampled currents by the designed frequency-converting DSOGI structure without time-variable physical parameters. Based on this structure, the influences of the unnecessary harmonics caused by these effects are reduced during the model building and prediction processes since they are effectively filtered, and an accurate data-driven model of the plant is online built based on the cleaned currents. Under the conditions of parameter mismatches and inserted harmonics due to the effects, the proposed method shows advantages such as reduced influences of the effects and improved quality of the phase currents according to the experimental and simulation results compared to the MF-PCC strategy, while maintaining its high robustness against parameter mismatches.

The proposed method has the potential to improve the data-driven model quality of the model-free predictive control on principle. However, since the model-free predictive control based on the look-up table (LUT) has a different building process, the proposed method should be further modified to improve the accuracy of the continuously updating LUT.

References

[1] M. Abu-Ali, F. Berkel, M. Manderla, S. Reimann, R. Kennel, and M. Abdelrahem, "Deep learning-based long-horizon MPC: Robust, high performing and computationally efficient control for PMSM drives," *IEEE Trans. Power Electron.*, vol. 37, no. 10, pp. 12486–12501, Oct. 2022, doi: 10.1109/TPEL.2022.3172681.

[2] X. Zhang and Z. Zhao, "Multi-stage series model predictive control for PMSM drives," *IEEE Trans. Veh. Technol.*, vol. 70, no. 7, pp. 6591–6600, Jul. 2021.

[3] P. Karamanakos, M. Nahalparvari, and T. Geyer, "Fixed switching frequency direct model predictive control with continuous and discontinuous modulation for grid-tied converters with LCL filters," *IEEE Trans. Control Syst. Technol.*, vol. 29, no. 4, pp. 1503–1518, Jul. 2021.

[4] F. Wang, S. Li, X. Mei, W. Xie, J. Rodríguez, and R. M. Kennel, "Model-based predictive direct control strategies for electrical drives: An experimental evaluation of PTC and PCC methods," *IEEE Trans. Ind. Informat.*, vol. 11, no. 3, pp. 671–681, Jun. 2015.

[5] C. Ma, J. Rodriguez, C. Garcia, and F. De Belie, "Integration of reference current slope based model-free predictive control in modulated PMSM drives," *IEEE J. Emerg. Sel. Topics Power Electron.*, early access, doi: 10.1109/JESTPE.2022.3159586.

[6] F. Wang, H. Xie, Q. Chen, S. A. Davari, J. Rodríguez, and R. Kennel, "Parallel predictive torque control for induction machines without weighting factors," *IEEE Trans. Power Electron.*, vol. 35, no. 2, pp. 1779–1788, Feb. 2020.

[7] Y. Wei, Y. Wei, Y. Sun, H. Qi, and X. Guo, "Prediction horizons optimized nonlinear predictive control for permanent magnet synchronous motor position system," *IEEE Trans. Ind. Electron.*, vol. 67, no. 11, pp. 9153–9163, Nov. 2020.
[8] A. Favato, P. G. Carlet, F. Toso, R. Torchio, and S. Bolognani, "Integral model predictive current control for synchronous motor drives," *IEEE Trans. Power Electron.*, vol. 36, no. 11, pp. 13293–13303, Nov. 2021.
[9] P. F. C. Gonçalves, S. M. A. Cruz, and A. M. S. Mendes, "Disturbance observer based predictive current control of six-phase permanent magnet synchronous machines for the mitigation of steady-state errors and current harmonics," *IEEE Trans. Ind. Electron.*, vol. 69, no. 1, pp. 130–140, Jan. 2022.
[10] M. S. Mousavi, S. Alireza Davari, V. Nekoukar, C. Garcia, and J. Rodriguez, "Integral sliding mode observer-based ultra-local model for finite-set model predictive current control of induction motor," *IEEE Trans. Emerg. Sel. Topics Power Electron.*, vol. 10, no. 3, pp. 2912–2922, Jun. 2021, doi: 10.1109/JESTPE.2021.3110797.
[11] F. Wang, J. Wang, R. M. Kennel, and J. Rodríguez, "Fast speed control of AC machines without the proportional-integral controller: Using an extended high-gain state observer," *IEEE Trans. Power Electron.*, vol. 34, no. 9, pp. 9006–9015, Sep. 2019.
[12] Z. Song, F. Zhou, and Z. Zhang, "Parallel-observer-Based predictive current control of permanent magnet synchronous machines with reduced switching frequency," *IEEE Trans. Ind. Informat.*, vol. 15, no. 12, pp. 6457–6467, Dec. 2019.
[13] Z. Hou and T. Lei, "Constrained model free adaptive predictive perimeter control and route guidance for multi-region urban traffic systems," *IEEE Trans. Intell. Transp. Syst.*, vol. 23, no. 2, pp. 912–924, Feb. 2022.
[14] J. Li, S. Wang, Z. Hou, and J. Zhao, "Multivariable model-free adaptive controller design with differential characteristic for load reduction of wind turbines," *IEEE Trans. Energy Convers.*, vol. 37, no. 2, pp. 1106–1114, Jun. 2021, doi: 10.1109/TEC.2021.3125112.
[15] M. Khalilzadeh, S. Vaez-Zadeh, J. Rodriguez, and R. Heydari, "Model-free predictive control of motor drives and power converters: A review," *IEEE Access*, vol. 9, pp. 105733–105747, 2021.
[16] X. Yuan, Y. Zuo, Y. Fan, and C. H. T. Lee, "Model-free predictive current control of SPMSM drives using extended state observer," *IEEE Trans. Ind. Electron.*, vol. 69, no. 7, pp. 6540–6550, Jul. 2022.
[17] Y. Zhang, J. Jin, and L. Huang, "Model-free predictive current control of PMSM drives based on extended state observer using ultralocal model," *IEEE Trans. Ind. Electron.*, vol. 68, no. 2, pp. 993–1003, Feb. 2021.
[18] N. Jin, M. Chen, L. Guo, Y. Li, and Y. Chen, "Double-vector model-free predictive control method for voltage source inverter with visualization analysis," *IEEE Trans. Ind. Electron.*, vol. 69, no. 10, pp. 10066–10078, Oct. 2021, doi: 10.1109/TIE.2021.3128905.
[19] Y. Wei, H. Young, F. Wang, and J. Rodríguez, "Generalized data-driven model-free predictive control for electrical drive systems," *IEEE Trans. Ind. Electron.*, early access, doi: 10.1109/TIE.2022.3210563.
[20] R. Heydari et al., "Model-free predictive control of grid-forming inverters with LCL filters," *IEEE Trans. Power Electron.*, vol. 37, no. 8, pp. 9200–9211, Aug. 2021, doi: 10.1109/TPEL.2022.3159730.
[21] D. Wang et al., "Model predictive control using artificial neural network for power converters," *IEEE Trans. Ind. Electron.*, vol. 69, no. 4, pp. 3689–3699, Apr. 2022.
[22] H. Mesai-Ahmed, I. Jlassi, A. J. Marques Cardoso, and A. Bentaallah, "Model-free predictive current control of synchronous reluctance motors based on a recurrent neural network," *IEEE Trans. Ind. Electron.*, vol. 69, no. 11, pp. 10984–10992, Nov. 2021, doi: 10.1109/TIE.2021.3120480.
[23] Y. Luo and C. Liu, "A simplified model predictive control for a dual three-phase PMSM with reduced harmonic currents," *IEEE Trans. Ind. Electron.*, vol. 65, no. 11, pp. 9079–9089, Nov. 2018.
[24] S. Dai, J. Wang, Z. Sun, and E. Chong, "Multiple current harmonics suppression for low-inductance PMSM drives with deadbeat predictive current control," *IEEE Trans. Ind. Electron.*, vol. 69, no. 10, pp. 9817–9826, Oct. 2022.
[25] T. Li, R. Ma, and W. Han, "Virtual-vector-Based model predictive current control of five-phase PMSM with stator current and concentrated disturbance observer," *IEEE Access*, vol. 8, pp. 212635–212646, 2020.
[26] W. Song, C. Xue, X. Wu, and B. Yu, "Modulated finite-control-set model predictive current control for five-phase voltage-source inverter," *IEEE Trans. Transport. Electrific.*, vol. 7, no. 2, pp. 718–729, Jun. 2021.
[27] Q. Liu, Y. Ying, and M. Wu, "Extended harmonic resonance analysis of grid-connected converters considering the frequency coupling effect," *IEEE Trans. Ind. Electron.*, vol. 69, no. 9, pp. 9353–9363, Sep. 2022.
[28] Y. Wang, Q. Xu, and J. M. Guerrero, "Effect of frequency coupling on stability analysis of a grid-connected modular multilevel converter system," *Energies*, vol. 14, no. 20, pp. 6580, Oct. 2021.
[29] R. Sreejith and B. Singh, "Sensorless predictive current control of PMSM EV drive using DSOGI-FLL based sliding mode observer," *IEEE Trans. Ind. Electron.*, vol. 68, no. 7, pp. 5537–5547, Jul. 2021.
[30] T. Zhang, X. Mei, and X. Du, "Absolute position acquisition for linear synchronous motor with passive mover," *IEEE Access*, vol. 9, pp. 100757–100768, 2021.
[31] Z. Xin, R. Zhao, F. Blaabjerg, L. Zhang, and P. C. Loh, "An improved flux observer for field-oriented control of induction motors based on dual second-order generalized integrator frequency-locked loop," *IEEE J. Emerg. Sel. Topics Power Electron.*, vol. 5, no. 1, pp. 513–525, Mar. 2017.
[32] J. Rodriguez and P. Cortes, *Predictive Control of Power Converters and Electrical Drives*, 1st ed. Chichedter, U.K.: Wiley, 2012.

Fengxiang Wang (Senior Member, IEEE) was born in Jiujiang, China, in 1982. He received the B.S. degree in electronic engineering and the M.S. degree in automation from Nanchang Hangkong University, Nanchang, China, in 2005 and 2008, respectively, and the Ph.D. degree in electrical engineering from the Institute for Electrical Drive Systems and Power Electronics, Technische Universitaet Muenchen, Munich, Germany, in 2014.

Currently, he is a Full Professor and Deputy Director with the Quanzhou Institute of Equipment Manufacturing, Haixi Institutes, Chinese Academy of Sciences, Jinjiang, China. His research interests include predictive control and sensorless control for electrical drives and power electronics.

Dr. Wang serves as an IET Fellow, and an Associate Editor for IEEE TRANSACTIONS ON INDUSTRIAL ELECTRONICS and IEEE TRANSACTIONS ON ENERGY CONVERSION. As General Chair, he organized the IEEE 5th International Symposium on Predictive Control of Electrical Drives and Power Electronics (PRECEDE).

Yao Wei (Member, IEEE) was born in Handan, China, in 1993. He received the B.S. and Ph.D. degrees in power electronics and power transmission from Yanshan University, Qinhuangdao, China, in 2015 and 2021, respectively. He is currently working toward the Postdoctoral project in material science and engineering with the Quanzhou Institute of Equipment Manufacturing, Haixi Institutes, Chinese Academy of Sciences, Jinjiang, China.

His research interests include driving and advanced control for electric vehicles and servo systems.

He serves as a Senior Member of China Electrotechnical Society (CES) and a Member of Chinese Society for Electrical Engineering (CSEE).

Hector Young (Senior Member, IEEE) was born in Valparaiso, Chile, in 1984. He received the B.Eng. and M.Sc. degrees in electronics engineering from the Universidad de la Frontera, Temuco, Chile, both in 2009, and the Ph.D. degree in power electronics from the Universidad Tecnica Federico Santa Maria, Valparaiso, Chile, in 2014.

Since 2014, he has been an Assistant Professor with the Electrical Engineering Department, Universidad de La Frontera. His research interests include modeling and control of power converters and electrical drives, renewable energy systems, and microgrids.

Dongliang Ke (Senior Member, IEEE) was born in Quanzhou, China, in 1986. He received the B.S. degree in electrical engineering and the M.S. degree in power electronics and power drives from Northwestern Polytechnical University, Xi'an, China, in 2010 and 2013, respectively.

Currently he is a Postdoctoral Supervisor, Deputy Director with Electrical Drives Laboratory, and Senior engineer with the Quanzhou Institute of Equipment Manufacturing, Haixi Institutes, Chinese Academy of Sciences, Jinjiang, China. His research interests include predictive control, flux-oriented control, sensorless control, and identification for electrical drives and power converters.

He serves as an IET Member and Member of the Chinese Society for Electrical Engineering. He also served as Session Chair of the IEEE 5th International Symposium on Predictive Control of Electrical Drives and Power Electronics (PRECEDE).

Haotian Xie (Member, IEEE) was born in Jiangsu Province, China, in 1990. He received the B.S. and M.Sc. degrees in electronic engineering from the Nanjing University of Aeronautics and Astronautics, Nanjing, China, in 2013 and 2017, respectively. He is currently working toward the Ph.D. degree in electrical engineering with the Chair of Electrical Drive Systems and Power Electronics and the Chair of High-Power Converter Systems, Technical University of Munich, Munich, Germany.

His research interests include modern predictive control, and sensorless control for electrical machine drive system.

José Rodríguez (Life Fellow, IEEE) received the engineering degree from the Universidad Tecnica Federico Santa Maria, Valparaiso, Chile, and the Dr.-Ing. degree in from the University of Erlangen, Erlangen, Germany, in 1977 and 1985, respectively, both in electrical engineering.

Since 1977, he has been with the Department of Electronics Engineering, Universidad Tecnica Federico Santa Maria, where he was Full Professor and President. From 2015 to 2019, he was the President of Universidad Andres Bello, Santiago, Chile. Since 2022, he has been the President of Universidad San Sebastian, Santiago, Chile. He has authored or coauthored two books, several book chapters, and more than 700 journal and conference papers. His main research interests include multilevel inverters, new converter topologies, control of power converters, and adjustable-speed drives.

Dr. Rodriguez was the recipient of a number of best paper awards from journals of the IEEE. In 2014, he was the recipient of the National Award of Applied Sciences and Technology from the government of Chile, and in 2015 he was the recipient of the Eugene Mittelmann Award from the Industrial Electronics Society of the IEEE. He is member of the Chilean Academy of Engineering. In years 2014 to 2021, he has been included in the list of Highly Cited Researchers published by Web of Science.